Research Article Vol. 12, No. 4 / April 2025 / Optica 479

Raman flow cytometry using time-delay integration

Matthew Lindley,[1,†] Toshiki Kubo,[1,2,†] Stéphanie Devineau,[1,3] Menglu Li,[1] Jing Qiao,[1] Takuya Yashiro,[4,5] Shiroh Iwanaga,[6] Kazuyo Moro,[4,5,7] and Katsumasa Fujita[1,5,8,*]

[1]Department of Applied Physics, Osaka University, 2-1 Yamadaoka, Suita, Osaka 565-0871, Japan
[2]Department of Dermatology, Course of Integrated Medicine, Graduate School of Medicine, Osaka University, 2-2 Yamadaoka, Suita, Osaka 565-0871, Japan
[3]Université Paris Cité, CNRS, Unité de Biologie Fonctionnelle et Adaptative, 75013 Paris, France
[4]Laboratory for Innate Immune Systems, Graduate School of Medicine and IFReC, Osaka University, 2-2 Yamadaoka, Suita, Osaka 565-0871, Japan
[5]Institute for Open and Transdisciplinary Research Initiatives, Osaka University, 2-1 Yamadaoka, Suita, Osaka 565-0871, Japan
[6]Department of Molecular Protozoology, Research Institute for Microbial Diseases, Osaka University, 3-1 Yamadaoka, Suita, Osaka 565-0871, Japan
[7]Laboratory for Innate Immune Systems, RIKEN-IMS, 1-7-22 Suehiro-cho, Tsurumi-ku, Yokohama, Kanagawa 230-0045, Japan
[8]AIST-Osaka University Advanced Photonics and Biosensing Open Innovation Laboratory, National Institute of Advanced Industrial Science and Technology (AIST), 2-1 Yamadaoka, Suita, Osaka 565-0871, Japan
[†]These authors contributed equally to this work.
*fujita@ap.eng.osaka-u.ac.jp

Received 9 December 2024; revised 10 March 2025; accepted 11 March 2025; published 2 April 2025

Raman flow cytometry offers chemically sensitive, label-free measurement of cells and particles; however, the technique suffers from low cell throughput due to the weak Raman signal. Here, we demonstrate the use of time-delay integration (TDI) to achieve Raman flow cytometry combined with dual-sided line illumination. The use of line illumination from both sides of the cell flow capillary kept the cell stream in the detection area by balancing optical force from the illumination lines. The TDI allowed the accumulation of Raman signals from flowing cells without sacrificing the spectrum readout rate. With the developed system, we achieved Raman flow cytometry at throughputs of 32 and 78 events per second for cell and particle detection, respectively. We applied the technique for analyzing biological cells and successfully detected lipid uptake in HepG2 cells and degranulation in bone-marrow-derived murine mast cells. Our TDI Raman flow cytometry approach improves the throughput of Raman-spectroscopy-based cell analysis and extends its applicability to a wider range of biomedical research.

https://doi.org/10.1364/OPTICA.551480

1. INTRODUCTION

Chemically sensitive flow cytometry enables rapid identification and quantification of cellular phenotype for large cell samples at single-cell resolution. It is widely used in biological, medical, and industrial fields, where applications include cell phenotyping, disease discovery, and rare cell detection [1]. Commonly in these applications, flow cytometry distinguishes phenotype by detecting exogenous fluorophore "labels" that are bound to target content within the cell or by associating transgenic fluorescent protein expression with target cellular processes. While this has enabled numerous advancements in understanding cell biology, such methods can suffer from non-specific labeling, cell toxicity, and incompatibility with therapeutic applications. These challenges have given rise to "label-free" flow cytometry, which identifies target chemical content in the cell via its direct interaction with light.

Raman flow cytometry seeks to realize label-free measurement of intracellular content by detecting the inelastic scattering of light from molecular vibration. In this process, the scattered light is given an energy shift, referred to as "Raman shift," that is conserved by the gain or loss of molecular vibration in the sample. The energies of these vibrational modes are determined by molecular structure, which allows Raman spectroscopy to produce a spectrum that serves as a "fingerprint" for identifying molecules in a specimen. Raman flow cytometers have been used to detect phenotype based on intracellular carotenoid [2,3], polysaccharide [4,5], and lipid and protein content [3,6,7], as well as to analyze cell metabolism [2,3], drug resistance [3], differentiation [6], size [8], and morphology [9]. Additionally, several Raman flow cytometers have been equipped with real-time analysis and mechanical response to allow Raman-activated cell sorting based on enzyme function [10,11], intracellular chemical content [12,13], and morphology [7].

For Raman flow cytometers, one of two kinds of Raman scattering spectroscopy is employed: spontaneous or coherent. Spontaneous Raman scattering spectroscopes are typically less expensive and simpler to build. However, they produce weak signals due to the low cross section of Raman scattering, which is roughly 15 orders of magnitude smaller than that of fluorescence [14]. Because of this, measurement usually requires a few hundred milliseconds of acquisition for strongly scattering targets up to

several seconds of acquisition for weakly scattering targets. To facilitate such long acquisition times, spontaneous Raman flow cytometers and flow-based sorters have relied on trapping cells during measurement [3,10–12,15–17]. This adds significant complexity to the cytometers and reduces throughput. To the best of our knowledge, spontaneous Raman flow cytometers demonstrated to date are limited to throughputs of less than 5 events/s [3], where an event is defined as the detection and measurement of a cell, cell cluster, or cell-sized debris. Raman scattering signal can be enhanced by using resonance Raman measurement, which relies on strong optical absorption by the analyte to increase scattering probability, but this limits addressable analytes to strongly absorbing intracellular chemicals such as carotenoids and chlorophyll [18]. Thus, low throughput has remained a bottleneck for spontaneous Raman flow cytometers, preventing applications requiring rapid analysis or rare cell detection. A second type of Raman scattering spectroscopy, called coherent Raman scattering spectroscopy, makes use of pulsed lasers to drive a vibrational coherence in the sample during measurement. For short acquisitions, this produces much better signal-to-noise ratios than spontaneous Raman measurement, though at typically increased cost and experimental complexity. The use of coherent Raman scattering has allowed throughputs up to ∼2000 events/s in Raman flow cytometers [2]; however, coherent Raman flow cytometers to date are limited by a smaller spectral bandwidth compared to their spontaneous Raman counterparts, which reduces the number of chemical species they can detect.

Here, we demonstrate the use of time-delay integration (TDI) to overcome the throughput bottleneck of spontaneous Raman-based flow cytometry while maintaining its broadband spectral content. TDI is a technique developed to counteract motion blurring of an image as it transits the face of a charge-coupled device (CCD) array during signal acquisition. It accomplishes this by shifting the photoelectrons integrated during a continuous acquisition along the CCD array at a rate that matches the motion of the sample's image (Fig. 1A), with the caveat that the velocity of the image is uniform and unidirectional. TDI was first demonstrated in astronomy [19], with subsequent use in radiographic and CT imaging [20], capillary electrophoresis [21], and fluorescence flow cytometry [22]. By applying TDI to Raman flow cytometry, we demonstrate a trapping-free spontaneous Raman flow cytometer capable of cell measurement of various cell types at up to 32 events/s and particle measurement at 78 events/s, with a spectral range from spanning the fingerprint, silent, and CH-stretch Raman regions ($500-3300\ \mathrm{cm}^{-1}$) with a spectral resolution of $<5\ \mathrm{cm}^{-1}$. We typify our flow cytometer's performance with the measurement of microplastic particles and different cell types, namely, HeLa cells, hepatocytes, mast cells, and red blood cells. Then we demonstrate the analysis of lipid accumulation in HepG2 cells grown under different culture conditions. Finally, we discuss the theoretical limits to throughput with this regime.

2. EXPERIMENTAL SETUP

Our flow cytometer consisted of three parts: the optical illumination line, the optical detection line, and the flow path, as shown in Fig. 1B. The optical illumination line contained a high-power 532 nm continuous-wave (CW) laser with optics that shaped the beam into a light sheet, aligned such that the long axis of its focal waist was colinear with the flow path. We calculated light sheet intensity in the focal region to range from 0.26 to 3.2 $\mathrm{mW}/\mu\mathrm{m}^2$ depending on laser output settings, based on a simulation of beam geometry and power measurements at the sample position. The light sheet imparted a force upon flowing particles and cells in the direction of optical propagation, which tended to push the sample out of alignment with the measurement region at high optical power. We attribute this force to radiation pressure by the light sheet, which we calculate at 55 pN for a 3.0 μm bead illuminated at 3.2 $\mathrm{mW}/\mu\mathrm{m}^2$, resulting in a maximum velocity of 1.9 mm/s in the direction of light sheet propagation [23]. To counteract the radiation pressure, we retroreflected the illumination line, as shown in Figs. 1C and 1D, such that the flowing sample was illuminated (pushed) from both sides.

We collected the scattering signal using an objective lens mounted orthogonally to the light sheet's propagation and long focal waist axes. We used a tube lens, dichroic mirror, and relay lenses to carry the Raman scattering signal from the objective to a spectrometer equipped with a cooled CCD camera oriented so that the images of flowing cells traveled along the spectrometer slit. We then oriented the spectrometer's CCD array to align its TDI axis (400 pixels) colinearly with motion in the imaging plane. We used the CCD array's orthogonal axis (1340 pixels) as the Raman shift axis following dispersion by the spectrometer's grating.

The measurement region in our flow cytometer can be modeled as a product of the point-spread functions (PSFs) of our illumination and detection optics. We designed the image magnification at the CCD camera to be low (4.8 to 9.6 times) so that the signal from a relatively large volume within the sample could be integrated in a single CCD pixel, with the goal of minimizing readout noise per signal. Figure 1E shows a model of the intensity distribution of the excitation light sheet at the measurement position. A model of our detection PSF, based on system optics, slit width, and CCD pixel size, is shown in Fig. 1F. The product of these two volumes gives the effective measurement region, shown in Fig. 1G. For TDI measurement of Raman scattering from the cells, it was imperative that the cells traveled along the measurement region. We flowed cells through a square quartz capillary (outer width and height 600 μm, channel width and height 240 μm) using acoustic focusing from an attached piezoelectric transducer to confine cell motion to the center of the capillary (Fig. 1A) and then adjusted the capillary position relative to the light sheet to align the cell motion with the measurement region.

A brief theoretical treatment of throughput in the setup follows. The acquisition time τ is given by the time it takes a cell image to transit the length of the CCD array, such that $\tau = \frac{L}{R}$, where L is the pixel number along the TDI axis and R is the spectral rate (here, we assume a well-controlled flow speed matches the image transit across the CCD face to the spectral rate). Throughput T maximizes as $T = \frac{N}{\tau} = \frac{NR}{L}$, where N is the expectation value of the number of cells that can be distributed along the CCD's TDI axis. This number is initially determined by the sample concentration but also increases as magnification is reduced. Ideally, at low magnification, the entire signal from a cell is confined to just one pixel width along the direction of TDI transit. Distributing signal from a single cell among a minimum number of pixels also carries the benefit of minimizing the CCD readout noise per event. In an optimal case, single cells could be distinguished by two pixels in a cell-blank-cell-blank pattern along the TDI axis, where $N = \frac{L}{2}$. In such a case, maximum throughput becomes dependent only on the spectral rate, $T_{\max} = \frac{R}{2}$, provided that the CCD array is long enough for acceptable signal accumulation and

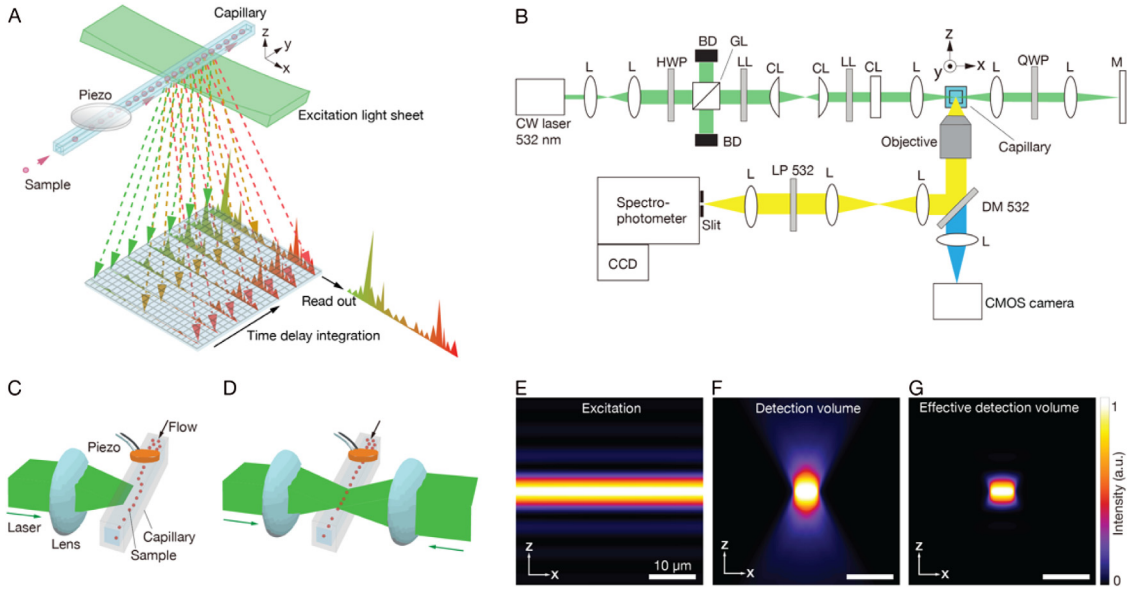

Fig. 1. Diagram of TDI Raman flow cytometer and optics simulations. (A) TDI Raman flow cytometry scheme. (B) Optical layout; L, CL, HWP, GL, BD, LL, QWP, M, DM, SP, and LP are lens, cylindrical lens, half-wave plate, Glan-laser calcite polarizer, beam dump, laser line filter, quarter-wave plate, mirror, dichroic mirror, short-pass edge filter, and long-pass edge filter, respectively. The direction of flow is along the y direction. (C), (D) Illustration of flow path with (C) one- and (D) two-way illumination. The cell flow is focused to the capillary center using a piezo transducer. When having one-way illumination, the laser pushes cells out of alignment with the measurement region. Applying counter-propagating illumination enables balancing the pressure on the cells. (E)–(G) Simulated distribution of (E) intensity of excitation light sheet, (F) detection volume given by the convolution product of the detection PSF and confocal slit, and (G) effective detection volume considering both excitation and detection volumes. We assumed a slit width of 50 μm, which corresponds to 5.2 μm at the object space.

the cell distribution is well controlled. However, for the simple flow channel and acoustic focusing design used in this experiment, the spatial distribution of cells along the flow axis was not controlled. Under such cases, intercell spacing is commonly modeled using a Poisson distribution, $P(k) = \frac{\left(\frac{N}{L}n\right)^k e^{-\frac{N}{L}n}}{k!}$, where $P(k)$ is the probability that k cells are observed in a pixel interval n, provided there is no cell-to-cell influence. In this regime, the single-cell event throughput is $\frac{NR}{L} \cdot P(1)$, and $P(1)$ maximizes at 37%.

3. RESULTS

To validate the spectral measurement by our Raman flow cytometer using TDI, we measured ethanol spectra by a side-illumination Raman spectrophotometer with and without using TDI, and a conventional confocal Raman spectrophotometer and confirmed identical spectra in each mode, as shown in Fig. S1. Following spectral verification, we next typified flow-based spectral acquisition using polystyrene beads, which commonly serve as standards in the Raman flow cytometry due to their uniform size and shape, strong Raman signal, and commercial availability. Measuring 3 μm diameter beads, we achieved a sustained throughput of 78 events/s. The bead sample was prepared at 6×10^6 particles/mL, though analysis of the high-speed video shows an average of 116 particles/s, equivalent to 3.3×10^6 particles/mL, transiting the capillary. We attribute the reduction in number density between sample preparation and measurement to beads settling out of suspension in the pump reservoir during the setup and execution of the flow cytometry.

The difference in particle count between our high-speed video and our spectrometer can be explained by comparing their temporally aligned data. An image composited from three frames of high-speed video of beads undergoing measurement is shown in Fig. 2A. In the image, the beads flow from right to left, and the direction of light sheet propagation is from top to bottom for the initial illumination. The beads scattered a higher portion of this light than the flow media, causing them to appear as white particles against a dark background in the image. The spectral readout of Raman scattering from the beads, as captured by our TDI spectrometer, is shown in Fig. 2B, following background removal and denoising. Here, an increase in baseline intensity indicates a particle transit event. The spectral data in Fig. 2B were captured simultaneously with the video data in Fig. 2A, and the data have been arranged to temporally align in the figure. Pink arrows indicate beads flowing far enough apart that their spectra could be easily resolved as separate events. The blue arrow indicates two beads clumped together such that their spectra begin to overlap temporally. Additionally, imperfect acoustic focusing allowed some beads to transit the measurement region at the edge of the light sheet where they were largely outside the collection optics PSF. Scattering from these out-of-focus beads (an example is indicated by the green arrow) appears in the high-speed camera images but was largely rejected by the slit of our spectrometer, which provided a high sectioning capability. The characteristic fingerprint-region peaks of polystyrene around 1000 cm^{-1}, 1600 cm^{-1}, and the CH-stretch region peaks on either side of 3000 cm^{-1} are readily apparent in the spectra of in-focus beads but missing for out-of-focus beads.

We tested two algorithms for detecting and counting events in the spectral data, as detailed in Fig. 2C, which shows in green the integrated signal intensity from 3040 to 3072 cm^{-1} acquired by the spectrometer for the temporal region corresponding to Figs. 2A and 2B. Our first event selection algorithm defined events by a simple intensity threshold, where single events were denoted by

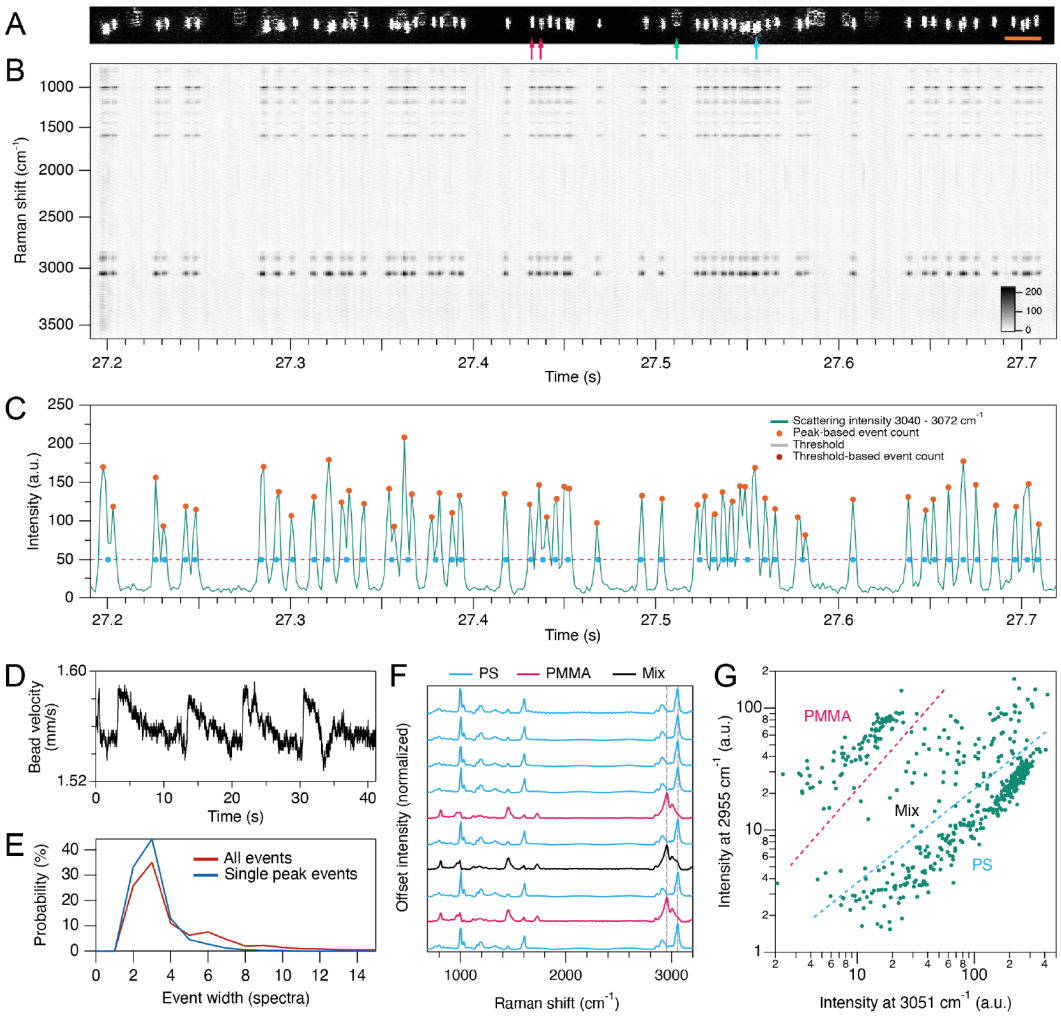

Fig. 2. High-throughput measurement of PS microbeads and measurement of a mixed PS-PMMA beads sample. (A) Images of 3 μm polystyrene beads flowing in capillary at ∼138 beads/s, captured by a high-speed camera. Scale bar 30 μm. Pink and blue arrows denote successive beads that can be distinguished or not be distinguished as individual events, respectively, in the spectral readout. The green arrow indicates a bead flowing outside the optical focal plane. (B) Corresponding spectral readout from flow cytometer after denoising. (C) Integrated scattering signal, with events selected by a peak-based algorithm (orange circles) or a threshold-based algorithm (blue circles). (D) Spectral width of events at the threshold for all events ($N = 2323$). (E) Histogram of event width at threshold indicated in (C). (F) Successive single-event spectra from a mixed PS and PMMA sample. Vertical gray lines show peak positions plotted in (G). (G) Scatter plot of Raman shift intensity at the primary PS and PMMA peaks in the CH-stretch region.

a signal rising above and then falling below an arbitrarily chosen threshold value, shown by the gray line in Fig. 2C. Events selected by this algorithm are displayed by a blue dot at the temporal center of the event, and we assigned an event spectrum for each event by averaging its above-threshold spectra. Our threshold-based algorithm often combined spectra from multiple beads into a single event, particularly for a low threshold value, so we developed a more robust peak-based event selection algorithm. This peak-based algorithm defined the signal as the average scattering intensity from 3040 to 3072 cm^{-1} and selected as an event any spectrum that was above threshold and was both preceded and followed by spectra with lower intensity values. Single-event spectra were then averaged from the set of 3 to 11 spectra (as set by the user) spanning each peak position. Example peak selection from this algorithm is shown by the orange dots in Fig. 2C.

The data chosen for Figs. 2A–2C consist of a temporal region of data with many beads in immediate proximity to one another, making the data useful for judging TDI performance as throughput is maximized. The composite image shows 68 beads transiting the measurement region in 0.5 s (from 27.2 to 27.7 s), equivalent to 136 beads/s. Of these, 12 beads (18%) are out of focus, leaving 56 beads (112 beads/s) capable of being spectrally detected. The temporally aligned TDI spectral readouts in Figs. 2B and 2C show our threshold-based algorithm detecting 42 events (84 events/s) and our peak-based algorithm detecting 52 events (104 events/s). For the latter, two events are "multi-bead" events in which the spectra from two closely spaced beads are indistinguishable, giving a yield of 96% for single-bead events. The data shown in Figs. 2A–2C were selected as the extreme case from a dataset of 41 s of continuous measurement, across which threshold-based selection reported a throughput of 56 events/s and peak-based selection returned 78 events/s. These results from peak-based selection are quite close to the theoretical treatment of throughput at this spectral rate and bead number density for a pixel interval of 3, which matches the bead diameter. Under these parameters, theory suggests a throughput of 72 events/s, with a

single-bead yield of 37% of spectra and 78% of events. The higher rate of single-bead event yield in our empirical data suggests that bead-to-bead interactions pushed us out of the Poisson regime.

The TDI scheme relies on the image velocity being uniform and matching the spectral rate of the TDI spectrometer. We analyzed bead velocity through the measurement region by tracking their horizontal displacement in the high-speed video data using a frame-to-frame cross-correlation algorithm. These results are shown in Fig. 2D. We found that bead velocity averaged 1.56 mm/s with a standard deviation of 13 μm/s. We show the temporal pattern in Fig. 2D because we believe it correlates with pressurization cycles in our sample pump. With perfect flow-TDI matching, signal from a 3 μm PS bead would distribute across two to three pixels along the TDI axis of the spectrometer (9.96× magnification produced an image width of 30 μm on the CCD, which had a pixel width of 20 μm). A histogram of the spectral widths of the 2323 events detected by our threshold algorithm, displayed in Fig. 2E, shows that 78% of single peak events had a spectral width of two to three spectra, as selected by our threshold. For the 22% of peak events larger than two to three spectra, we believe that flow-TDI rate mismatch during the pump pressurization cycle played a role, along with contributions from beads too clustered to distinguish individual peaks. We further explored the effect of a flow-TDI rate mismatch on spectral quality and peak intensity by flowing PS beads at set pump rate while varying the TDI spectral rate, with results shown in Fig. S2.

We next flowed a mixed sample of PS (3 μm) and PMMA (4 μm) beads, collecting 503 event spectra at a throughput of eight events/s. PMMA had a weaker Raman signal than PS, necessitating a reduction in the TDI spectral rate to 465 Hz to increase acquisition time, which was expected to yield 64% of the throughput we showed with PS beads. The mixed bead sample was prepared at 6× lower concentration than the pure PS sample, which further reduced throughput. Additionally, although the sample was prepared at a 1:1 PS:PMMA concentration, the higher density of PMMA beads resulted in relatively more PMMA settling out of solution, producing a lower number of PMMA events in our measurement. Figure 2F shows single-event spectra from these data, with PS in cyan and PMMA in pink, as determined by their spectral profiles. In the data, 66% of events were identified as PS, 17% as PMMA, and 17% as mixed PS-PMMA events. We show an example of a mixed spectra in black in the figure. A scatterplot of peak intensity at the PMMA peak location at 2955 cm^{-1} versus the PS peak location at 3051 cm^{-1} is shown in Fig. 2G. The pure-species events in these data show good separation in the scatter plot. Examples of raw data and denoised spectral data are shown in Fig. S3 of Supplement 1. Our denoising algorithm is described in Section 5 with examples in Fig. S4 of Supplement 1.

We next demonstrated flow cytometry with fixed HeLa cells at a throughput of 32 events/s. To accommodate the width of HeLa cells (up to ∼40 μm), the flow cytometer detection line was configured with a 20× 0.45 NA objective, resulting in a total magnification of 4.8× to confine the cell signal to fewer pixels along the TDI axis. Figure 3A shows scattering intensity versus time for the HeLa sample under flow conditions. Figure 3B shows a zoomed section of the data in Fig. 3A. Most events consisted of a single narrow peak along the temporal axis, which we attribute to the passage of one cell through the measurement region. Wider events with multiple peaks were likely due to the passage of clumped cells. Our threshold-based algorithm selected 323 events and our peak-based algorithm selected 438 events based on scattering intensity from 2921 to 2953 cm^{-1}, with an example of these selections shown by blue and orange dots, respectively, in the figure. Each event spectrum was averaged from all above-threshold event spectra for threshold-based event selection, and from the five contiguous spectra spanning and centered on the peak position for peak-based selection. Examples of these spectra, corresponding to the lowercase alphabet index (a, b, c, …), are shown in Fig. 3C after spectral processing. Examples of raw and processed spectra from the HeLa dataset are shown in Fig. S5 of Supplement 1 and processed spectra of live-cell measurement of HeLa in Fig. S6 of Supplement 1. Each spectrum shows fingerprint region peaks commonly attributed to cytochromes (750 and 1585 cm^{-1}), phenylalanine (1004 cm^{-1}), lipids (1085 and 1458 cm^{-1}), amide III bonds (1252 cm^{-1}), and amide I bonds (1669 cm^{-1}), among other peaks. Additionally, each event shows strong intensity in the high-wavenumber region that is associated with CH_2 vibration in lipids (2862 and 2931 cm^{-1}) and CH_3 vibration in proteins (2931 cm^{-1}). For these HeLa cell data and the later murine mast cell data, cytochromes have a resonant Raman response to our illumination wavelength of 532 nm; however, the other molecules listed above do not. Figure 3D shows a scatterplot of maximum intensity (signal height) versus integrated intensity (total signal) for threshold-selected events. We expected the ratio of these values to distinguish single-cell events from cell-cluster events in the data, and color coded these data by the number of peaks per event. The color coding showed strong grouping between event width and peak number, suggesting that the ratio of peak intensity to area could be used as a gating metric to distinguish single-cell events. Cell diameters of 20 to 40 μm, commonly reported for HeLa, should produce single-cell event widths of 5–10 spectra, which are observed in these data. We note some event widths from the one peak group in Fig. 3D are larger than 10 spectra. Contributing factors to larger widths may include cell diameters larger than 40 μm, single-peaked cell cluster events, fluctuations in flow rate, defocusing of the cell image on the CCD, or a combination of these factors.

HeLa cells are typically large, making them comparatively easy to acoustically focus and they give a strong Raman signal. To test the robustness of the flow cytometer when measuring other cell types, we next flowed fixed murine mast cells, which typically are sized between 10 and 15 μm. We have found during Raman microscopy that mast cells have a weak Raman signal and very high background autofluorescence compared to other cell types. For the mast cell measurement, we successfully captured 18,636 events at 17 events/s, based on peak picking at 2910−2974 cm^{-1}. Example single-event spectra and a sample average spectrum are shown in Fig. 3E, following background removal and denoising. Additional raw and denoised spectral data from mast cell measurement are shown in Figs. S7B and S8B of Supplement 1. Finally, to demonstrate resonance Raman measurement, we flowed human erythrocytes, which feature strong resonance Raman scattering from hemoglobin at our 532 nm illumination wavelength. We captured 7289 events at a throughput of 27 events/s, based on peak picking at 1537−1599 cm^{-1}, with single-event spectra and a sample average spectrum shown in Fig. 3F, with additional spectral data shown in Fig. S9 of Supplement 1. With the strong resonance Raman signal in this measurement, it is likely we could have significantly increased throughput by reducing magnification

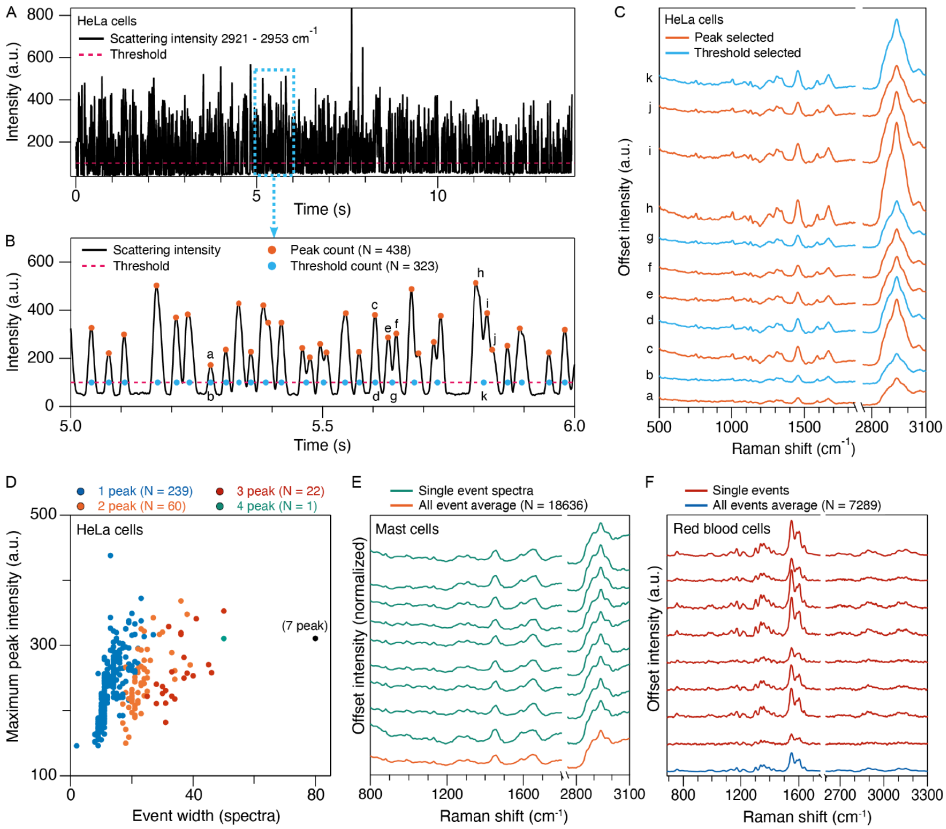

Fig. 3. High-throughput measurement of cells. (A) Integrated signal intensity from HeLa cells under flow. (B) Integrated signal intensity from 5.0 to 6.0 s showing threshold and event selection by threshold algorithm (blue dots) and peak picking algorithm (orange dots). Throughputs measure 24 and 32 events/s, respectively. (C) Single-event spectra for peaks indicated in (B) by lowercase letters. (D) Example of single-cell gating using a scatter plot of maximum signal intensity versus event width. Colors are assigned by intra-event peak count. (E) Successive single-event spectra and sample average from mast cell measurement. Throughput during the measurement averaged 17 events/s. (F) Successive single-event spectra and sample average from erythrocytes. Spectral profile is dominated by the resonance Raman response of hemoglobin. Throughput during the measurement averaged 27 events/s.

power. As it was, for this acquisition, we reduced laser power to 4%–6% of the level used for normal cell measurements, resulting in an intensity of 130 $\mu W/\mu m^2$ at the light sheet waist.

As an application demonstration, we analyzed the lipid content of the human HepG2 hepatocyte cell line following treatment with 0.2 mM free fatty acid (FFA). Cells were cultured under two conditions. These consisted of a control sample and a sample with FFA in the growth media using bovine serum albumin (BSA) as a carrier. More than 2100 events for each condition were analyzed by our flow cytometer, with the average spectrum from each condition shown in Fig. 4A. An increased lipid signal at 2862 cm^{-1} can be observed in the FFA sample. To distinguish this fatty acid accumulation at the single-event level, we applied principal component analysis–linear discriminant analysis (PCA–LDA). PCA was first applied, and the first principal components (PCs) contributing 95% were selected. Then we trained a linear discrimination analysis (LDA) model on the data sets reconstructed by the selected PCs; 5/6 of the data was used as a randomly selected training set, and model accuracy was validated against the remaining 1/6 of the data, yielding a classification accuracy of 89%. We show the plot of LDA scores in Fig. 4B. We found stable flow conditions more difficult to establish with the HepG2 cells, with cells consistently catching and collecting at the inlet to capillary. This problem was somewhat mitigated by reducing the pump rate, but our effective throughput during measurement was reduced to two events/s. The reduced pump rate necessitated a TDI spectral rate of 465 Hz. We next used our flow cytometer to distinguish granulated and degranulated murine mast cells at a throughput of 17 events/s and at our maximum spectral rate of 729 Hz. Mast cells are granulocytes that play a role in the inflammatory immune system by releasing histamines from intracellular storage granules in response to pathogens, parasites, or allergens. Averaged spectra from all events for granulated and degranulated samples are shown in Fig. 4C. PCA–LDA classification distinguished the samples with an accuracy of 81%. We show the LDA scores in Fig. 4D. Example single-event spectra from the HepG2 and mast cell measurements are shown in Fig. S7 of Supplement 1, and raw data are shown in Fig. S8 of Supplement 1.

4. DISCUSSION AND CONCLUSION

We demonstrated TDI Raman flow cytometry at throughputs of up to 32 events/s, with spectra that span the fingerprint and high-wavenumber regions. This is a significant improvement in throughput for Raman flow cytometers at this spectral bandwidth (500−3400 cm^{-1}) and resolution (<5 cm^{-1}). The spectra show peaks commonly assigned to Raman vibrational modes of phenylalanine (1004 cm^{-1}), lipids (1450 cm^{-1}, 2850 cm^{-1}), amide III bonds (1252 cm^{-1}), and amide I bonds (1669 cm^{-1}), and proteins (2931 cm^{-1}), as well as resonant Raman vibrational modes in cytochromes (750 cm^{-1}). We were able to measure a

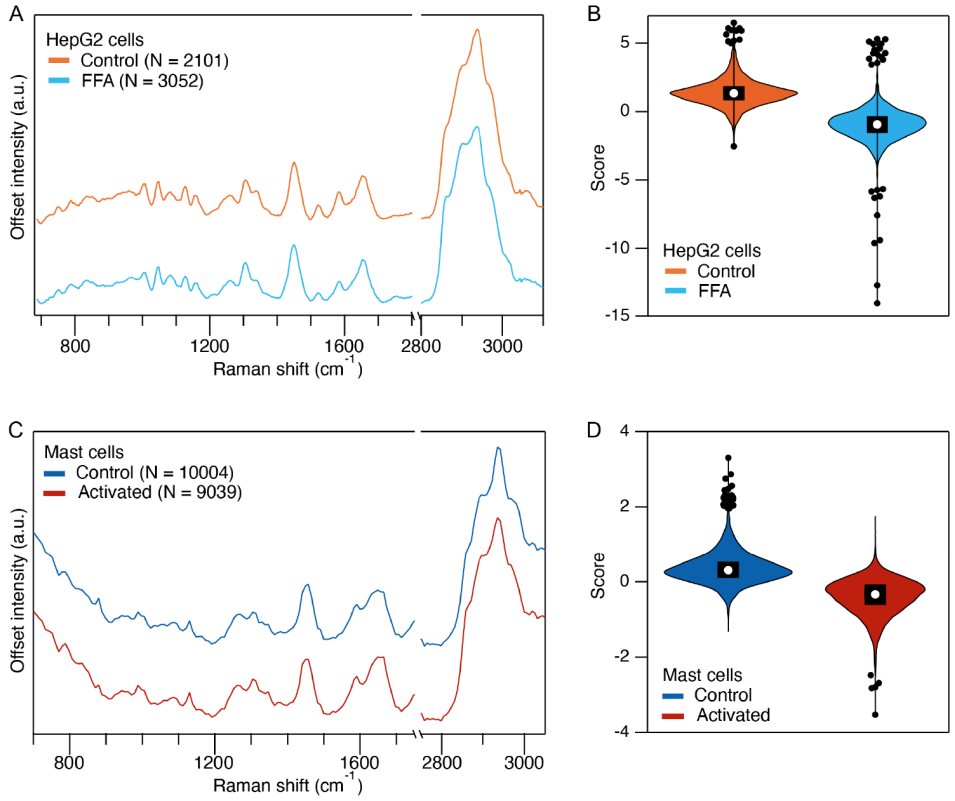

Fig. 4. Measurement of lipid content in HepG2 cells. (A) Averaged spectra from HepG2 cells cultured in media with free fatty acid (FFA) and without (control), as measured by our flow cytometer. (B) Classification of HepG2 control and FFA sample Raman flow cytometry events using linear discriminant analysis. Classification accuracy was 89%. (C) Averaged spectra from granulated (control) and degranulated (activated) mast cells. (D) Classification of mast cell Raman flow cytometry events using linear discriminant analysis. Classification accuracy was 81%. For (B) and (D), the black boxes show the interquartile range with white circles at the medians. Black circles denote far outliers. Throughput during the measurement was 2 events/s for HepG2 samples and 17 events/s for mast samples (see Visualization 1, Visualization 2 and Visualization 3).

range of mammalian cell types and sizes, including cells with high fluorescent background, and the label-free nature of Raman flow cytometry obviated the need for staining and allowed samples to be measured after minimal preparation. In our case, preparation usually consisted of an optional cell fixation step, then resuspension for adherent cells, followed by a simple concentration or dilution step to adjust the suspension to an appropriate number density, which was on the order of 10^6 cells/mL.

In our current setup, the detection speed is limited by the readout speed of the CCD camera. For the high-throughput cell and bead data presented in Figs. 2 and 3, we ran our TDI CCD at its maximum spectral rate of 729 spectra/s. Sample flow speed, and thereby throughput, improves linearly with this rate, and we expect to be able to demonstrate yet higher throughputs by switching to a faster CCD, with newer commercially available models providing a 2× to 8× improvement at the time of this writing, suggesting sustained throughputs of 100 events/s and higher are possible.

Regarding flow-TDI rate matching, our data in Figs. 2D and 2E show that our flow cytometer undergoes periodic shifts in flow rate due to the pump's pressurization cycle. A desync between flow rate and TDI rate has two effects. First, it distributes the event signal across a greater number of pixels. As each additional pixel contributes readout noise to the event measurement, this decreases the SNR. Additionally, cells that are temporally close to each other can have their signals mixed, as a mismatched TDI rate will shift an accumulating pixel from an initial cell onto its temporal neighbor, increasing the rate of multi-cell events. Thus, a pump that minimizes pressure fluctuations would improve the performance of the flow cytometer for both SNR and single-cell event yield. A second solution could be to monitor flow speed in real time via our high-speed imaging camera and adjust the TDI rate to match, though we have not examined the availability of CCDs with adjustable readout rates during acquisition.

Another improvement to our flow cytometer can be realized in its data handling. Currently, we capture up to 200,000 successive spectra (~4.5 min) before saving data, during which data acquisition is halted. This means that large-scale acquisitions such as our mast cell data are stitched together from several successive data acquisitions for analysis in post processing. Developing seamless data transfer from the TDI spectrometer to the control software would allow longer measurements. Additionally, it would allow real-time analysis and control necessary to implement Raman-activated cell sorting. We report our event throughputs as the average event rate during active measurement for an entire dataset and did not factor in the downtime between repeats for large samples. We note that while best practice dictates that throughput should also consider such downtimes [24], we believe focusing on throughput during measurement is a better way to judge the potential of TDI at this proof-of-concept stage. Additionally, an agitation mechanism to keep particles and cells suspended for longer measurements will be needed. Continuous agitation in

the sample reservoir could particularly improve throughput for denser-than-water samples such as PMMA.

Overcoming the random inter-bead spacing described by the Poisson distribution offers a way to further increase throughput. Along similar lines, work to create uniform cell distributions along microfluidic channels has been undertaken in the field of droplet encapsulation for cells [25], where it has been demonstrated that more uniform event distributions are possible through careful modification of the flow channel. We note that encapsulating single cells in a uniformly spaced droplet array very much resembles the encapsulation of single-cell images within uniformly spaced TDI pixels, and we believe the techniques to overcome the Poisson distribution utilized in droplet microfluidics can be extended to TDI flow cytometry (with or without droplets) to further increase single-cell throughput.

Though we demonstrated the measurement of live HeLa cells, we did not typify cell viability following measurement. We leave the exploration of live-cell yield, an important consideration for the extension of TDI to cell sorting, to future works. An inverse relation between a cell's viability and its optical absorption coefficient at the flow cytometer's illumination wavelength is expected. We calculate illumination intensity in our measurements to be $0.52-6.4\ \mathrm{mW}/\mu\mathrm{m}^2$ (depending on the sample) at the light sheet's 7 μm beam waist for an exposure of up to 1 s per cell volume. We note that our previous demonstrations of live-cell compatible line-illumination Raman microscopy typically used an intensity of $1.0-3.0\ \mathrm{mW}/\mu\mathrm{m}^2$ and a total exposure time of 2–5 s per cell volume, which is a similar order of total exposure to our flow cytometer [26–28].

Detection limits in Raman microscopy are typically in the millimolar range for intracellular molecules (outside of the resonance Raman regime) but vary by analyte [29]. Since analyte concentration can also vary significantly depending on cell type and culture conditions, it would be reasonable to compare with slit-scanning Raman microscopy that uses line illumination to discuss the sensitivity with TDI detection. Both regimes illuminate the sample with a line focus and project the Raman scattering signal to a CCD spectrometer that encodes position along the line focus onto one CCD axis and Raman shift onto the orthogonal CCD axis. This gives the basis for comparable sensitivity between the regimes. Our TDI flow cytometer, however, uses lower magnification ($5\times-10\times$ TDI flow versus $20\times-60\times$ imaging), which results in a theoretical four-fold or greater increase in signal photon count per pixel compared to the Raman microscopy setups previously built [26–28], given similar illumination intensity, detection volume, CCD pixel size, and signal collection efficiency. The trade-off for this is the lack of spatial resolution in TDI-flow cytometry, and the fact that SNR reduces when flow and TDI rates are mismatched or when the coincidence of the flow path and measurement region is poor. Considering those conditions, the detection sensitivity in our TDI Raman cytometry remains at a millimolar level. The slower flow may improve the sensitivity, making more difficult precise flow focus for efficient signal detection.

Sensitivity is also an important factor of analysis methodology, although it is difficult to precisely discuss due to the sample and its condition dependency. Considering the comparable exposure conditions, the sensitivity of our system is also expected to be comparable with line-illumination spontaneous Raman microscopy. Therefore, single-cell analysis should be available at a similar sensitivity to that we performed during microscopy [26–28]. The lower magnification of our TDI system may also provide a higher sensitivity, though optical parameters may be further improved. In our experiments, we set the slit width to 50 μm, corresponding to 2.5 pixels on the CCD camera, ensuring a consistent spectral resolution across all samples. However, under these conditions, Raman detection efficiency is not always optimized for different sample sizes. To maximize detection sensitivity, adjusting the magnification of the detection optics to account for the sample size is essential. Additionally, in most Raman flow cytometry reports, the size of the signal generation volume at the optical focus is smaller than the cell volume. This should be considered for future applications and may be overcome by enlarging the illumination and detection volume.

We expect the broad spectral range of TDI Raman detection to also be compatible with labeled flow cytometry using Raman tags and isotopic labels. Significant efforts have gone toward developing such tags [30–32], and their narrow Raman peak structures allow dozens of "colors" to be distinguished, enabling highly multiplexed labeling of intracellular content.

We have demonstrated TDI-Raman flow cytometry at >30 events/s, which is a $6\times$ improvement in throughput for cell measurement spanning the fingerprint and high-wavenumber region. Our result indicates that further significant improvements to throughput can be achieved using the TDI method with modifications to camera rate and microfluidic channel design, pushing throughput above 100 cells/s without sacrificing spectral range or analyte sensitivity. We expect this to further open Raman flow cytometry to high-throughput cell analysis and cell sorting applications.

Raman spectroscopic flow cytometry has potential applications in medical and biological research, as well as in clinical settings. Our demonstration of successive detection of free fatty acid (FFA) uptake in HepG2 cells suggests the possibility of identifying fatty liver cells, which could be valuable for studying metabolic-dysfunction-associated fatty liver disease [33] and for liquid biopsy to detect circulating tumor cells, which is reported exhibiting higher lipid signals compared to normal cells [34], Additionally, our system holds promise for studying diseases related to mast cells. Since conventional degranulation detection methods rely on fluorescent labeling, our system offers a label-free alternative in this field. Another potential application is the diagnosis of bloodstream infections. Current bacterial detection methods are slow, as they require incubation of blood samples before analysis. Given that the risk of mortality increases within 12 h of blood collection, yet conventional methods take 12 to 48 h [35], a faster detection system is crucial. However, sensitivity remains a challenge, as Raman signals from bacteria are typically weaker than those from larger cells. Our system could also be applied to the detection of malaria-infected blood [36]. For blood sample applications, the resonant signal from red blood cells must be carefully evaluated, as it may either enhance or interfere with the detection of significant signals. In cases where interference occurs, the use of near-infrared excitation light could be a solution. Furthermore, our system may be useful for the label-free evaluation of stem cells for cell therapy applications [37].

5. MATERIALS AND METHODS

A. Cytometer Design

The optical setup configuration is as described in Fig. 1. A 532 nm CW laser (Millenia-eV 25 W, Spectra Physics) was used for the excitation light source. The beam was collimated by a beam expander that consists of two lenses (AC254-050-A-ML and AC254-200-A-ML, Thorlabs). We controlled beam power by the combination of a half-wave plate (WPH10M-532, Thorlabs) and a Glan-laser calcite polarizer (10GL08AR.14, Newport). The beam size in the z direction was individually adjusted by a pair of cylindrical lenses ($f = 200$ and ACY254-050-A, Thorlabs) to tune the effective excitation NA, and shaped into a sheet by the combination of a cylindrical lens (LJ1567RM, Thorlabs) and a spherical lens (AC254-030-A-ML, Thorlabs). The laser passing through the quartz capillary (Noel) was collected by a lens pair (AC254-030-A-ML and AC254-075-ML, Thorlabs) having a quarter-wave plate (WPQ10M-532, Thorlabs) in between. The laser beam was reflected by a mirror back to the capillary to balance the optical force on samples and align the flow path. We utilized the quarter-wave plate to rotate the polarization of the retroreflected beam by 90 deg in total so that it was directed by the Glan prism to the beam dump and did not enter the laser cavity. The Raman scattering was collected by an objective lens (Plan Fluor ELWD 40× 0.6 NA or 20× 0.45 NA, Nikon) and imaged by a tube lens (G063204000, Linos). After reflection by a 546 nm short-pass edge filter (FF01-546/SP-25, Semrock), the signal transited a relay system (ACT508-250-A-ML, Thorlabs and AC508-075-A-ML, Thorlabs) with an edge long-pass edge filter (LP03-532-RU-50, Semrock) between the relay lenses and was imaged on a spectrophotometer (CLP-100, Bunkoukeiki). After dispersion by a grating (1200 grooves/mm grating blazed at 500 nm) inside the spectrometer, the Raman spectra were imaged on a cooled CCD camera (PIXIS 400BR, Teledyne). High-speed video imaging utilized a Memrecam Q2M (nac Imaging Technology) containing a complementary metal oxide semiconductor image sensor (ST-865, nac Image Technology).

B. Flow System

We used a pressure pump (P-pump, Dolomite Microfluidics) with an integrated flow sensor for consistent sample flow. A square quartz capillary (Square Capillary 1, Nakahara Opto-Electronic Laboratory, Inc) was used at the measurement region due to the reduced background of quartz compared to glass for Raman measurement. Flow out after the capillary was routed to a waste container. Cells and particles in flow were acoustically focused by a piezoelectric transducer (Fuji Ceramics, 3.089Z6D-SY) affixed to the capillary with super glue. We drove the transducer with a 3.096 MHz sine wave output at 1 Vpp from a signal generator (WF1976, NF Corporation) and then amplified by a bipolar amplifier (HSA4101, NF Corporation).

C. Data Acquisition

Up to 200,000 spectra were recorded per measurement, equivalent to 4 min and 34 s of continuous data acquisition, after which acquisition was halted for a few minutes as data were saved on the control PC. To acquire larger datasets, we performed multiple successive measurements.

D. High-Speed Video Analysis

We calculated bead velocity using high-speed video data that consisted of successive frames of 1920 pixel × 40 pixel images recorded at 100 fps, where the beads traveled along the 1920 pixel axis. The algorithm first flattened the images to a 1920 × 1 pixel intensity profile using a maximum value function. Using these profiles, bead velocity at frame i was then calculated by a cross correlation between frame i-5 and $i + 5$, where the maximum value of the cross correlation gave the displacement in pixels during a 10-frame time interval. This displacement in pixels was then converted to distance using the camera pixel size and magnification.

E. Spectral Data Processing

Our post-processing of spectral data consisted of four steps: pixel-to-wavenumber calibration, quartz and water baseline removal, fluorescence background removal, and noise removal. The spectrometer camera captured 1340 pixels along its spectral axis as raw data, of which 800 pixels were used to span the fingerprint, cell silent, and high wavenumber Raman regions (205−3320 cm^{-1} for our HeLa data), as shown in Fig. S4A. Raman scattering from the quartz capillary produced small background peaks below 1000 cm^{-1}, while Raman scattering from water produced a peak at 1600 cm^{-1} and a very strong and broad peak at ∼3300 cm^{-1}. To isolate this baseline signal, we selected 200 spectra from event-free regions, then averaged these spectra and smoothed the result with an 11-pixel binomial filter. Figure S4B shows examples of an event-average spectrum and a non-event average spectrum taken from our data shown in Fig. S2A. We then subtracted this smoothed background from the raw data to remove the quartz and water Raman baseline, with the result shown in Fig. S4C in light blue, which captures the average of all spectra as a line and the standard deviation from all spectra as a shaded region. Autofluorescence background from the cells shows as a parabola-like intensity across the spectral region and is a major contributor to the large standard deviation. We then used a polynomial baseline removal algorithm to remove fluorescence background from the event data, the average of which is shown as the pink spectrum in Fig. S4C, with the standard deviation shown with pink shading. Next, we denoised the spectra using singular value decomposition (SVD). An example of this denoising result is shown for an example single event in Fig. S4D, where the denoised spectrum was constructed by keeping the first 52 singular values and setting the remainder to zero. The SVD scores and singular value matrix data are shown in Figs. S4E and S4F. For experiments comparing multiple samples, the SVD was applied to a single data matrix concatenated from all samples. Pixel-to-wavenumber calibration was performed by measuring neat ethanol flowing in the flow cytometer and fitting the pixel values of spectral peak locations to known ethanol Raman modes at 884, 1052, 1454, and 2931 cm^{-1} with a third-order polynomial. Given the weak signals in the mast cell data, we performed a two-pixel binning along the spectral axis before post processing. This improved SNR but reduced spectral resolution to $<10\ cm^{-1}$.

F. Illumination Intensities

Illumination intensities were 6.4 $mW/\mu m^2$ for mast and HepG2 cells, 4.6 $mW/\mu m^2$ for HeLa cells, 1.3 $mW/\mu m^2$ for microplastic

particles, and 0.26 mW/μm^2 for red blood cells. These intensities are given as the sum of the incident and retroreflected beams.

G. Particle Preparation

Standard microplastic concentrations were created by an initial dilution of commercial bead samples of known concentration (2.5% w/v 3 μm PS beads, Polysciences; 10% w/v 4 μm PMMA beads, Microparticles GmbH), followed by hand counting using a Neubauer chamber and an adjustment dilution as necessary. Our pure PS sample was prepared at 6×10^6 beads/mL and our mixed-bead sample was prepared with equal counts of PS and PMMA at a combined 1×10^6 beads/mL.

H. Cell Preparation

HeLa cells were cultured on a 25 mm^2 cell T-flask in Dulbecco's Modified Eagle Medium (DMEM, 043-30085, Wako-Fujifilm) supplied with 10% fetal bovine serum (FBS, S1780-500U, Biowest), and 1% penicillin–streptomycin–glutamine solution (15140122, Gibco) in a 5% CO_2 incubator at 37°C.

HepG2 cells were cultured in a minimum essential medium (MEM, 51200038, Thermo Fisher Scientific) supplemented with 10% fetal bovine serum (FBS, S1780-500U, Biowest), and 1% penicillin–streptomycin–glutamine solution (15140122, Gibco) in the CO_2 incubator at 37°C. On days two and three, we added different concentrations of FFA solutions (0 or 0.2 mM) to the HepG2 cell cultures. The FFA solutions were formulated by dissolving palmitic acid (P9767, Sigma-Aldrich) and oleic acid (O7501, Sigma-Aldrich) in a mole ratio of 1:2 into a culture medium containing 0.2 mM FFAs-free BSA. For measurement, HepG2 cells under each condition were collected into a 4 mL jar, and the medium was replaced with live cell imaging solution (A14291DJ, Thermofisher).

I. Culturing of BMMCs and Degranulation

Bone-marrow-derived mast cells (BMMCs) were generated by culturing bone marrow cells derived from a 10-week-old female C57BL/6NCrSlc mouse (Japan SLC) in an RPMI-1640 medium (R8758-500ML, SIGMA) supplemented with 10% fetal bovine serum, 10 mM HEPES, 1 mM sodium pyruvate, 55 μM 2-mercaptoethanol, 100 U/mL penicillin, 100 μg/mL streptomycin, and 10 ng/mL recombinant mouse IL-3 (554579, BD Pharmingen) for 4 weeks.

5×10^6 BMMCs were incubated with 200 ng/mL anti-TNP IgE (554118, BD Biosciences) for 2 h. After washing with 1× PBS, the cells were resuspended in 1× Tyrode buffer and then stimulated with or without 3 ng/mL TNP-BSA (LG-1117, LSL) for 1 h.

J. Erythrocytes

Erythrocytes and human serum were obtained from the Japanese Red Cross (research ID: 25J0143) with written informed consent. Erythrocytes were cultivated at 2% hematocrit in a complete medium, which consists of the RPMI-1640 medium containing 2.5% human serum, 2.5% AlbuMAX II (Life Technologies, Carlsbad, USA), 25 mM HEPES, 0.225% sodium bicarbonate, and 0.38 mM hypoxanthine supplemented with 10 μg/mL gentamicin. RBCs were incubated under low-oxygen conditions (90% N_2, 5% CO_2, and 5% O_2).

K. Cell Fixation

Cells were fixed in 4% paraformaldehyde and rinsed three times with a phosphate buffer solution.

L. Code

Processing of spectral and image data was performed using the custom code in Igor Pro (Wavemetrics) and MATLAB (Mathworks).

M. Statistical Analysis and Data Processing

Interquartile range and far outliers were calculated using the Tukey method in Igor Pro (Wavemetrics).

Funding. Japan Society for the Promotion of Science (22KF0235); Japan Science and Technology Agency (JPMJMI20G3, JPMJPF2009, JPMJKB2301).

Acknowledgment. The authors thank Dr. Kazuki Bando and Ryutaro Ohata for helping with optical setup construction. The authors also thank Taizo Koga for assistance with calculations.

Disclosures. MLindley, TK, and KF have a patent application related to this work (PCT/JP2024/003220). KF is a co-founder and the chief technology officer (CTO) of Millde Co., Ltd. The other authors have no competing of interests.

Data availability. All data needed to evaluate the conclusions in the paper are present in the paper and/or the supplementary materials.

Supplemental document. See Supplement 1 for supporting content.

REFERENCES

1. J. P. Robinson, "Flow cytometry: past and future," BioTechniques **72**, 159–169 (2022).
2. K. Hiramatsu, T. Ideguchi, Y. Yonamine, *et al.*, "High-throughput label-free molecular fingerprinting flow cytometry," Sci. Adv. **5**, eaau0241 (2019).
3. X. Wang, L. Ren, Z. Diao, *et al.*, "Robust spontaneous Raman flow cytometry for single-cell metabolic phenome profiling via pDEP-DLD-RFC," Adv. Sci. **10**, 2207497 (2023).
4. K. Hiramatsu, K. Yamada, M. Lindley, *et al.*, "Large-scale label-free single-cell analysis of paramylon in Euglena gracilis by high-throughput broadband Raman flow cytometry," Biomed. Opt. Express **11**, 1752–1759 (2020).
5. J. Gala De Pablo, M. Lindley, K. Hiramatsu, *et al.*, "Label-free live microalgal starch screening via Raman flow cytometry," Algal Res. **70**, 102993 (2023).
6. C. Zhang, K.-C. Huang, B. Rajwa, *et al.*, "Stimulated Raman scattering flow cytometry for label-free single-particle analysis," Optica **4**, 103–109 (2017).
7. N. Nitta, T. Iino, A. Isozaki, *et al.*, "Raman image-activated cell sorting," Nat. Commun. **11**, 3452 (2020).
8. H.-W. Wang, N. Bao, T. L. Le, *et al.*, "Microfluidic CARS cytometry," Opt. Express **16**, 5782–5789 (2008).
9. Y. Suzuki, K. Kobayashi, Y. Wakisaka, *et al.*, "Label-free chemical imaging flow cytometry by high-speed multicolor stimulated Raman scattering," Proc. Natl. Acad. Sci. USA **116**, 15842–15848 (2019).
10. K. S. Lee, M. Palatinszky, F. C. Pereira, *et al.*, "An automated Raman-based platform for the sorting of live cells by functional properties," Nat. Microbiol. **4**, 1035–1048 (2019).
11. X. Wang, Y. Xin, L. Ren, *et al.*, "Positive dielectrophoresis–based Raman-activated droplet sorting for culture-free and label-free screening of enzyme function in vivo," Sci. Adv. **6**, eabb3521 (2020).
12. P. Zhang, L. Ren, X. Zhang, *et al.*, "Raman-activated cell sorting based on dielectrophoretic single-cell trap and release," Anal. Chem. **87**, 2282–2289 (2015).

13. M. Lindley, J. Gala de Pablo, W. Peterson, *et al.*, "High-throughput Raman-activated cell sorting in the fingerprint region," Adv. Mater. Technol. **7**, 2101567 (2022).
14. S. Nie and S. R. Emory, "Probing single molecules and single nanoparticles by surface-enhanced Raman scattering," Science **275**, 1102–1106 (1997).
15. A. Y. Lau, L. P. Lee, and J. W. Chan, "An integrated optofluidic platform for Raman-activated cell sorting," Lab Chip **8**, 1116–1120 (2008).
16. C. Xie, D. Chen, and Y. Li, "Raman sorting and identification of single living micro-organisms with optical tweezers," Opt. Lett. **30**, 1800–1802 (2005).
17. W. E. Huang, A. D. Ward, and A. S. Whiteley, "Raman tweezers sorting of single microbial cells," Environ. Microbiol. Rep. **1**, 44–49 (2009).
18. Y. Lyu, X. Yuan, A. Glidle, *et al.*, "Automated Raman based cell sorting with 3D microfluidics," Lab Chip **20**, 4235–4245 (2020).
19. J. T. McGraw, J. R. P. Angel, and T. A. Sargent, "A charge-coupled device (CCD) transit-telescope survey for galactic and extragalactic variability and polarization," in *Applications of Digital Image Processing to Astronomy* (SPIE, 1980), Vol. **0264**, pp. 20–28.
20. D. W. Holdsworth, R. K. Gerson, and A. Fenster, "Scanned projection radiography with a slot beam," in *Medical Imaging II* (SPIE, 1988), Vol. **0914**, pp. 246–252.
21. M. E. Szulc and I. S. Krull, "Improved detection and derivatization in capillary electrophoresis," J. Chromatogr. A **659**, 231–245 (1994).
22. W. Hu, S. A. Soper, and J. M. Jackson, "Time-delayed integration–spectral flow cytometer (TDI-SFC) for low-abundance-cell immunophenotyping," Anal. Chem. **91**, 4656–4664 (2019).
23. A. Ashkin, "Acceleration and trapping of particles by radiation pressure," Phys. Rev. Lett. **24**, 156–159 (1970).
24. M. Herbig, A. Isozaki, D. Di Carlo, *et al.*, "Best practices for reporting throughput in biomedical research," Nat. Methods **19**, 633–634 (2022).
25. E. W. M. Kemna, R. M. Schoeman, F. Wolbers, *et al.*, "High-yield cell ordering and deterministic cell-in-droplet encapsulation using Dean flow in a curved microchannel," Lab Chip **12**, 2881 (2012).
26. K. Hamada, K. Fujita, N. I. Smith, *et al.*, "Raman microscopy for dynamic molecular imaging of living cells," J. Biomed. Opt. **13**, 044027 (2008).
27. M. Okada, N. I. Smith, A. F. Palonpon, *et al.*, "Label-free Raman observation of cytochrome *c* dynamics during apoptosis," Proc. Natl. Acad. Sci. USA **109**, 28–32 (2012).
28. M. Li, Y. Ueyama-Toba, M. Lindley, *et al.*, "Label-free evaluation of maturation and hepatotoxicity of human iPSC-derived hepatocytes using hyperspectral Raman imaging," Anal. Chem. **95**, 9252–9262 (2023).
29. D. Cialla-May, C. Krafft, P. Rösch, *et al.*, "Raman spectroscopy and imaging in bioanalytics," Anal. Chem. **94**, 86–119 (2022).
30. H. Yamakoshi, K. Dodo, A. Palonpon, *et al.*, "Alkyne-tag Raman imaging for visualization of mobile small molecules in live cells," J. Am. Chem. Soc. **134**, 20681–20689 (2012).
31. F. Hu, C. Zeng, R. Long, *et al.*, "Supermultiplexed optical imaging and barcoding with engineered polyynes," Nat. Methods **15**, 194–200 (2018).
32. R. Nishiyama, K. Hiramatsu, S. Kawamura, *et al.*, "Color-scalable flow cytometry with Raman tags," PNAS Nexus **2**, pgad001 (2023).
33. K. M. Helal, H. Cahyadi, J. N. Taylor, *et al.*, "Raman imaging of rat non-alcoholic fatty liver tissues reveals distinct biomolecular states," FEBS Lett. **597**, 1517–1527 (2023).
34. R. Mitra, O. Chao, Y. Urasaki, *et al.*, "Detection of lipid-rich prostate circulating tumour cells with coherent anti-Stokes Raman scattering microscopy," BMC Cancer **12**, 540 (2012).
35. L. Samuel, "Direct-from-blood detection of pathogens: a review of technology and challenges," J. Clin. Microbiol. **61**, e0023121 (2023).
36. A. Bonifacio, S. Finaurini, C. Krafft, *et al.*, "Spatial distribution of heme species in erythrocytes infected with Plasmodium falciparum by use of resonance Raman imaging and multivariate analysis," Anal. Bioanal. Chem. **392**, 1277–1282 (2008).
37. J. Ankrum and J. M. Karp, "Mesenchymal stem cell therapy: two steps forward, one step back," Trends Mol. Med. **16**, 203–209 (2010).